Molecular modelling of the heat capacity and anisotropic thermal expansion of nanoporous hydroxyapatite

Túlio Honório[a,1], Thibault Lemaire[a], Devis Di Tommaso[b], Salah Naili[a,*]

[a] *Laboratoire Modélisation et Simulation Multi Echelle, MSME UMR 8208 CNRS, Université Paris-Est, Créteil Cedex 94010, France*
[b] *Thomas Young Centre, Materials Research Institute and School of Biological and Chemical Sciences, Queen Mary University of London, Mile End Road, London E1 4NS, UK*

Abstract

~~The~~ Hydroxyapatite, which is the main mineral phase of mammalian bone, ~~hydroxyapatite, is characterised by nanopores where fluid can exist and flow.~~ occurs in the form of small bricks of colloidal size organized in a way that leaves room to micro-and mesopores. These pores are filled with an electrolyte and confined fluids are recognized for manifesting different dynamical and structural behaviors when compared to bulk fluids. Research on other nanoporous materials reported that confinement may have repercussions on the effective the thermal properties of these materials. Understanding the physical origin of thermal expansion and heat capacity as a function of the hydroxyapatite porosity is, therefore, crucial to predict the thermo-mechanical behavior of bone. Molecular dynamics simulations of hydroxyapatite nanopores ($2\ \text{nm} \leq \text{H} \leq 16\ \text{nm}$, where H is the size of the nanopore) in contact with liquid water have been used to determine the effect nanoporosity and water confinement on the heat capacity and thermal expansion of this important biomaterial. At temperatures corresponding to *in vivo* conditions, the thermal expansion of water confined in nanopores smaller than 6 nm was is solid-like but becomes liquid-like in larger nanopores. The heat capacity of confined water exhibits a

*Corresponding author
[1] *Present address*: LMT-Cachan/ENS-Cachan/CNRS/Université Paris Saclay, Cachan, France

maximum at pore sizes of approximately 7 nm. An up-scaling strategy taking into account the anomalous behaviour of nanoconfined water is then proposed to determine the effective heat capacity and the effective heat of hydroxyapatite expansion as a function of its porosity, and to predict regions of variability, compared with the bulk, ~~of~~ the thermal properties of porous hydroxyapatite.

Keywords: Hydroxyapatite; Confined water; Thermal expansion; Specific heat; Molecular dynamics; Homogenization.

---

1. Introduction

Properties such as thermal expansion and heat capacity characterize the behavior of mammalian bone under varying temperature conditions. In fact, despite ~~being~~ often assumed that bone is subject to small temperature variations, even subtle differences between the bone surface and deep-body zone temperatures might impact the local metabolism [1]. Moreover, orthopedic [2, 3, 4, 5] and odontological [6] interventions can to produce significant thermal effects. For instance, Jacobs et al. [6] observed temperature rises of at least 5°C in both graft bed and bone with dental burrs, and Krause et al. [3] reported clinical tests during total joint replacement operations in which temperatures exceed 200°C when irrigation was not used. Temperatures above 45°C were reported to cause thermal osteonecrosis [4, 5]. The recognition of the importance of these thermal effects goes back to Hippocrates' recommendation (500 BC) of frequently plunging the tools into cold water when trephining discs of bone from the skull to prevent the heating of the material [2, 7]. Healing following bone surgery may be delayed if the bone cells are injured by thermal effects [8]. From another perspective, thermal stimulation of tissues aiming at inducing localized necrosis has been proposed as a therapeutic tool [9]. However, relatively few experimental and theoretical studies have been concerned with the thermal properties of bone.

Hydroxyapatite (HAP), $Ca_{10}(PO_4)_6(OH)_2$, ~~is the main constituent phase of mineralized tissues found in mammalian bone, tooth enamel and dentin. HAP~~

can ~~then~~ be used as a proxy to study the thermal properties of bone. In these tissues, HAP occurs in the form of small "bricks" of colloidal size ~~[10]~~ [10, 11] organized in a way that leaves room to pores sizes ranging from 2 to 24 nm [12] in contact with body fluid. Confined water manifests different dynamical and structural behaviors when compared to bulk fluids (e.g. [13]), and research on other porous materials showed that nanoconfinement may have repercussions on their effective thermal properties [14, 15, 16, 17, 18, 19].

The molecular dynamics (MD) simulation technique is particularly suited to assess the behavior of water confined in nanopores as it allows ~~a~~ quantification of ~~the~~ interatomic forces and atomistic phenomena responsible for the anomalous behaviour of water, which otherwise would be difficult to probe experimentally, especially at the temperature and pressure corresponding to *in vivo* conditions [20]. Recent works of the authors using MD revealed important aspects of the structure and dynamics of water in HAP-water nanopores [21, 22, 23, 24], including the mechanisms controlling the anisotropic diffusion of water molecules within nanopores [25].

We anticipate that nanoporosity could also have a significant effect on the thermal properties HAP~~,~~ ~~But~~ despite its importance in biomechanic applications, to the best of the authors' knowledge~~,~~ no experimental or theoretical data is available regarding the role of nanoporosity on the thermal expansion and heat capacity. The MD technique has been ~~therefore~~ applied to compute the thermal expansion and heat capacity of bulk HAP and HAP-water nanopores with pore sizes ranging from 2 to 16 nm and to quantify the effect of water nanoconfinement ~~and~~ on the thermal properties of hydroxyapatite. An upscaling strategy based on homogeneization techniques is then used to link the anomalous thermal behaviour in HAP-water nanopores ~~because of confinement effects~~ to the effective thermal expansion and effective heat capacity of HAP as a function of its porosity.

2. Methods

2.1. Heat capacity and thermal expansion from molecular dynamics simulations

At the nanoscopic level, the heat capacity of a material is related to the vibrational modes of atoms (phonons), and the thermal expansion to the anharmonicity of the lattice interaction potential [26]. The heat capacity at constant strain C_ϵ quantifies how the internal energy U changes with temperature T:

$$C_\epsilon = \left(\frac{\partial U}{\partial T}\right)_{\epsilon_{ij}}, \tag{1}$$

where ϵ_{ij} are the components of the second-order Lagrangian deformation tensor $\boldsymbol{\epsilon}$ which is symmetric and associated with a reference volume V_0. In this paper, we adopt the convention that the subscripts as i, j and k which vary from 1 to 3 refer to Cartesian coordinates $\mathbf{x}, \mathbf{y}$ and $\mathbf{z}$ respectively (see Fig. 1). So, the indices 1, 2 and 3 map to **x**, **y** and **z** respectively. For a unit cell, the deformation tensor is defined by:

$$\boldsymbol{\epsilon} = \frac{1}{2}\left[\mathbf{h}_0^{-T}\mathbf{h}^T\mathbf{h}\mathbf{h}_0^{-1} - \mathbf{I}\right], \tag{2}$$

where $\mathbf{h}_0$ and $\mathbf{h}$ are two tensors associated with the metric of the reference and deformed unit cell, respectively, $\mathbf{I}$ is the unit tensor, and the superscript $[\star]^T$ denotes the transpose operator. Note that the unit cell is periodically repeated to fill all space whose the form and the volume are completely arbitrary but described by the 3 vectors $\mathbf{a}, \mathbf{b}$ and $\mathbf{c}$ that span the edges of the unit cell. This description can be obtained by arranging the vectors as $\{\mathbf{a}, \mathbf{b}, \mathbf{c}\}$ to form a (3,3) matrix $\mathbf{h}$ whose the columns are the components of $\mathbf{a}, \mathbf{b}$ and $\mathbf{c}$ (see Fig. 1) in this order.

The heat capacity at constant stress C_σ quantifies how the enthalpy changes with the temperature:

$$C_\sigma = \left(\frac{\partial H}{\partial T}\right)_{\sigma_{ij}} = \left(\frac{\partial (U + V_0 \mathrm{Tr}(\boldsymbol{\sigma}\boldsymbol{\epsilon}))}{\partial T}\right)_{\sigma_{ij}}, \tag{3}$$

where $\boldsymbol{\sigma}$ is the second-order Cauchy stress tensor which is symmetric and whose the components are denoted by σ_{ij} [27, 28, 29, 30] and Tr denotes the trace

operator of a tensor. The second-order thermal expansion tensor $\boldsymbol{\alpha}$ which is symmetric and defined by these components α_{ij} ~~which~~ quantify how the strain changes with the temperature under a constant stress:

$$\alpha_{ij} = \left(\frac{\partial \epsilon_{ij}}{\partial T} \right)_{\sigma_{ij}}. \tag{4}$$

The heat capacities C_σ and C_ϵ, and the elements of the thermal expansion tensor are related by the following expression [31]:

$$C_\sigma - C_\epsilon = V_0 T C_{ijkl} \alpha_{ij} \alpha_{kl}, \tag{5}$$

where C_{ijkl} is the fourth-order elastic stiffness tensor which is symmetric. In this paper, the Einstein summation convention is used which implies a summation over a set of indexed terms in a formula.

The heat capacities and the thermal expansion tensor have been computed from MD simulations ~~by means of~~ the fluctuation-dissipation formula. The fluctuation of two dynamical variables A and B is given by $\langle \delta A \times \delta B \rangle_{ens} = \langle AB \rangle_{ens} - \langle A \rangle_{ens} \langle B \rangle_{ens}$, where the operator $\langle \delta \star \rangle_{ens}$ denotes an ensemble average. In the isotension-isothermal (NσT) ensemble, the constant stress heat capacity can be computed from the fluctuations of the enthalpy H [32]:

$$C_\sigma = \frac{\langle \delta H^2 \rangle_{N\sigma T}}{kT^2}, \tag{6}$$

where k is the Boltzmann constant. In the isotension-isothermal (NσT) ensemble, the thermal expansion tensor can then be computed from the cross fluctuations of the strain and the enthalpy [27, 28, 30]:

$$\alpha_{ij} = \frac{\langle \delta \epsilon_{ij} \times \delta H \rangle_{N\sigma T}}{kT^2}. \tag{7}$$

The heat capacity at constant strain C_ϵ can be ~~then~~ computed using Eq. (5). Fluctuation-dissipation formula are particularly advantageous if one is interested in compute various properties or tensorial properties from a single simulation.

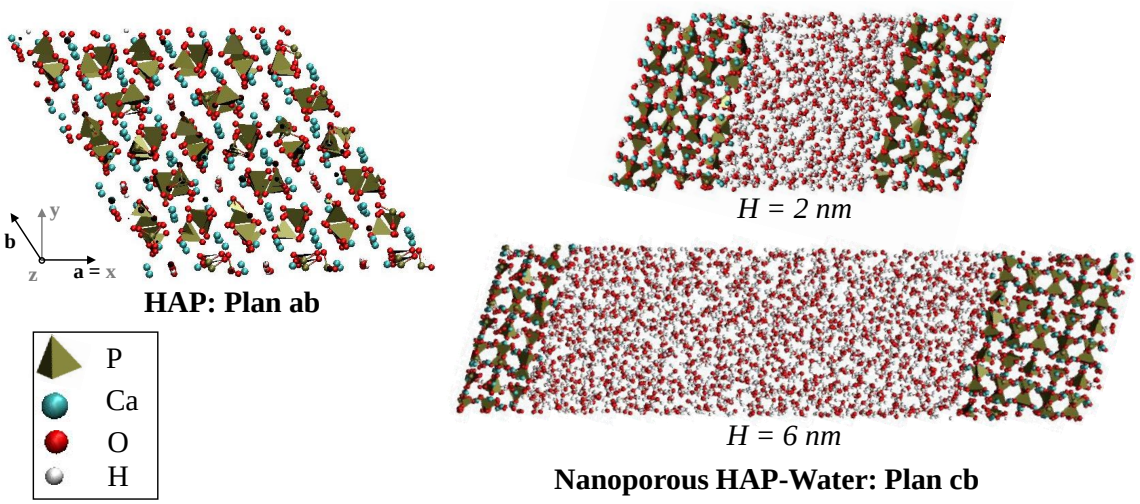

Figure 1: Snapshot of configuration of bulk HAP and HAP-water systems with $H = 2$ nm and $H = 6$ nm. For reference, the Cartesian coordinates $(\mathbf{x}, \mathbf{y}, \mathbf{z})$ and crystallographic $(\mathbf{a}, \mathbf{b}, \mathbf{c})$ frames are also shown.

2.2. Simulation details

The atomic structure of HAP was obtained from the hexagonal with $P6_3/m$ space group cell parameters of Sudarsanan and Young [33]. The simulation box is generated by stacking this unit cell 3 times in each in-plane direction and 4 times in out-of-plane direction (see Fig. 1), which results in a total number of atoms in the HAP solid layer of $N_{HAP} = 1584$ atoms.

For simulation of nanoporous HAP-water systems, HAP platelets were stacked with a surface-to-surface spacing along **c**-direction varying from 2 to 16 nm. The {0001} surface of HAP, which is the dominant surface in the thermodynamically-stable morphology [34], was considered as the basal plane. The slit pore was filled with water molecules at an experimental density of 1 g.cm^{-3}, which is close to the density of SPC/E water at ambient conditions.

The interatomic potential proposed by de Leeuw and co-workers [35, 36] to model crystalline apatite was used for HAP. In this force field, non-bonded interactions are described by Buckingham potentials, phosphate and hydroxyl group bonds as the sum of a Morse and a Coulombic potential, and phosphate bond

angles by a harmonic potential. The polarizability of oxygen anion in the phosphate and hydroxyl groups is described by a core-shell model. In HAP-water systems, water were modeled using the extended single-point charge (SPC/E) water model [37], and HAP-water interactions were described using non-bonded potentials derived in previous MD studies [38, 39].

MD simulations were performed using DL_POLY 4.05.1 code [40]. The systems were first equilibrated in the microcanonical (NVE) ensemble for 1 ns. Then, a first isotension-isothermal (NσT) run during 1ns was performed to equilibrate the system under a pressure of 1 atm and at a fixed temperature (from 290 to 330 K). The Nosé-Hoover thermostat and barostat, at relaxation time 500 fs for both, were used. Smoothed Particle Mesh Ewald (SPME) method with the acceptable relative error of 10^{-6} were employed to compute the long-range electrostatic interactions.

In order to verify the convergence of the estimations of the heat capacity and coefficients of thermal expansion, in the production phase the system was sampled for 2 ns in NσT ensemble (timestep of 1 fs). Figure 2 displays the fluctuations of the enthalpy, volume and deformations according to the in- and out-of-plane directions. To compute the deformations, the reference cell parameters defined via $\mathbf{h}_0$ (see Eq. (1)) were determined from the average at zero tension in NσT ensemble (*i.e.* in a state in which the deformation vanishes [41]). After approximately 1 ns the fluctuations yield smooth Gaussian distributions as shown in Fig. 2. From the estimations of the heat capacity, the isothermal compressibility and the coefficients of thermal expansion, we assume that a simulation run of 1 ns in isotension-isothermal ensemble captures the normal distribution of the thermodynamic quantities (**a**)-(**c**) and is enough to converge the results of the computed properties (**d**)-(**f**).

In this study, the pore size H is defined as the projection of **c** vector on the **z**-direction minus the effective thickness h_{HAP} of the solid HAP [21]. Following the definition of effective thickness and pore size used for other layered materials [42], h_{HAP} is defined as the distance between the center of the out-most oxygen (the out-most species in HAP surface) in each exposed HAP sur-

Table 1: Details of HAP-water systems. The number of atoms in HAP solid layer is N_{HAP} = 1584.

H (nm)	$\langle H \rangle$ (nm)	N_w
2	1.86	455
3	2.98	682
4	3.83	910
6	6.11	1363
8	7.97	1823
10	10.09	2276
12	12.16	2732
16	16.73	3650

face projected on **z**-direction plus twice the van der Waals radius of oxygen (r_O =0.152 nm). Correspondingly, the average pore size $\langle H \rangle_{N\sigma T}$ is computed by: $\langle H \rangle = \langle \mathbf{c}.\mathbf{z} \rangle_{N\sigma T} - \langle h_{HAP} \rangle_{N\sigma T}$. Table 1 displays the number of water molecules N_w for each target pore size H.

3. Results

3.1. Bulk HAP

Table 2 reports the heat capacity C_σ, the coefficients of the thermal expansion tensor α_{ii}, and the isothermal compressibility κ of bulk HAP computed from MD simulations at 300 K and compared to theoretical and experimental values reported in the literature. To obtain further validation of our atomistic model, we also computed the components of elastic stiffness tensor using the Parinello-Rahman fluctuation equation [43]:

$$C_{ijkl} = \frac{kT}{\langle V \rangle_{N\sigma T}} \left[\langle \delta\epsilon_{ij} \times \delta\epsilon_{kl} \rangle_{N\sigma T} \right]^{-1} .$$

The representation adopted in this paper is called the Voigt's representation in which the new indexes I et J vary in the set $\{1, ..., 6\}$ such as $I = (i, j)$ and

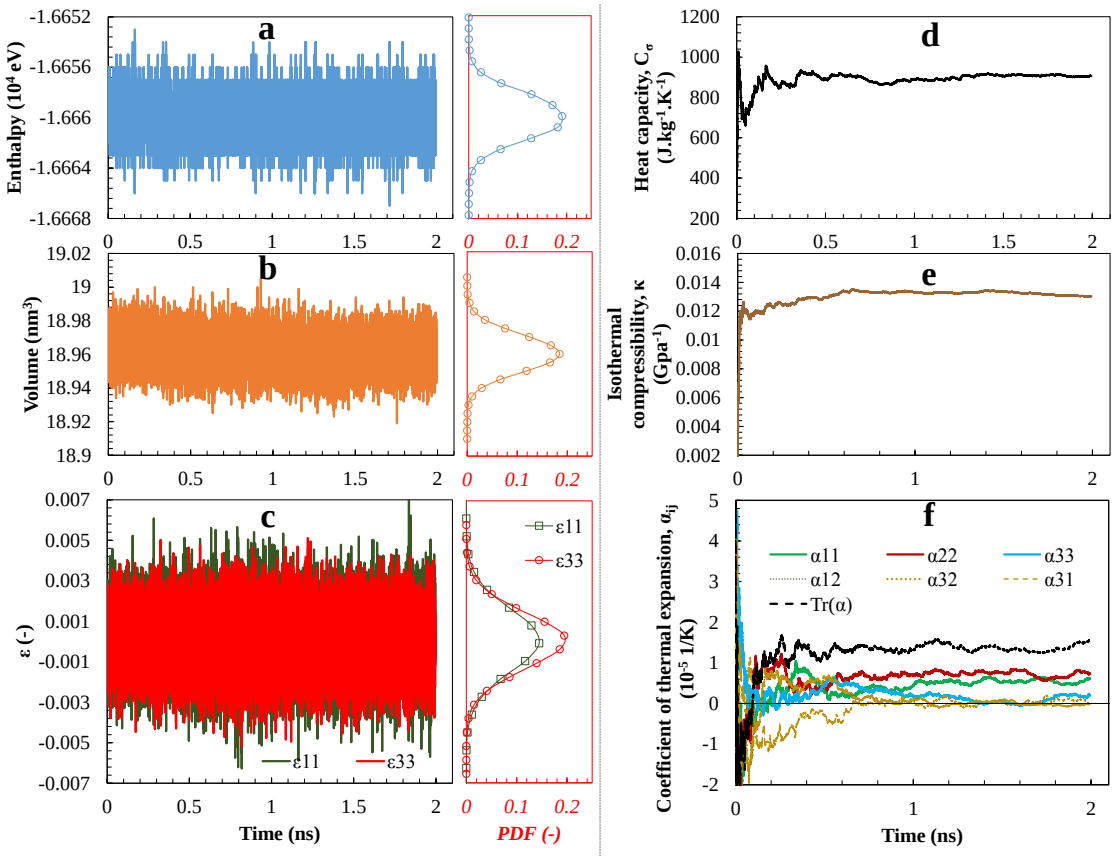

Figure 2: Convergence of thermodynamic quantities in bulk HAP at 310 K and under 1 atm. At left, the fluctuations of the (**a**) enthalpy, (**b**) volume, and (**c**) deformation along the **x** (11) and **z** (33) directions. At right, the variation of the (**d**) heat capacity, (**e**) isothermal compressibility (obtained from the fluations of the volume by [32]: $\kappa = \frac{\langle V^2 \rangle_{N\sigma T}}{kTV}$), and (**f**) coefficients of thermal expansion. For the latter, all components of the tensor $\boldsymbol{\alpha}$, computed from the fluctuations of the deformations with Eq. (7)) as well as its trace are reported shown.

Table 2: Heat capacity C_σ, coefficients of the tensor of thermal expansion α_{ii} and isothermal compressibility κ, and components of stiffness tensor C_{11}, C_{22} and C_{33} (Voigt notation) of bulk HAP at 300 K and under 1 atm. For comparison, results from the literature concerning, except otherwise indicated, experimental evaluation of hexagonal HAP at 300 K are provided.

	This work	Other works
C_σ (J.kg^{-1}.K^{-1})	875±72	768 [44]; 765 (298 K) [45]
		690 (MD 298 K) [46]
		632 (MD monoclinic 298 K) [46]
α_{11} ($\times 10^{-5}$ K^{-1})	0.68±0.50	0.39 [47]
α_{22} ($\times 10^{-5}$ K^{-1})	1.38±0.81	-
α_{33} ($\times 10^{-5}$ K^{-1})	1.31±0.32	1.86 [47]
$(1/3) \times \mathrm{Tr}(\boldsymbol{\alpha})$ ($\times 10^{-5}$ K^{-1})	1.13±1.01	1.82 (monoclinic 298 K) [48]
C_{11} (GPa)	97	140.0 [49] (ab initio); 117.1 [50]; 166.7 [51]; 115 [52]; 135 [53]
C_{22} (GPa)	93	134.8 [49] (ab initio)
C_{33} (GPa)	120	174.8 [49] (ab initio); 231.8 [50]; 139.6 [51]; 125 [52]; 172 [53]
κ (GPa^{-1})	0.013±0.004	0.0118 [49] (ab initio); 0.012 [50]; 0.016 [52]; 0.011 [53]

$J = (k, l)$ where the indices i, j, k and l vary in the set $\{1, ..., 3\}$. The relation between these indices is the following $1 = (1, 1), 2 = (2, 2), 3 = (3, 3), 4 = (2, 3), 5 = (1, 3)$ and $6 = (1, 2)$.

There is a general good agreement between the properties obtained from our simulations and the experimental values, which corroborates the transferability of the empirical force fields proposed by de Leeuw and co-workers [35, 36] for the computation of ~~the~~ thermal properties ~~of HAP~~.

Figure 3 shows the temperature dependence of the heat capacity at constant stress C_σ, isothermal compressibility κ, and elastic stiffness constants C_{11}, C_{22} and C_{33} (Voigt notation) of bulk HAP under 1 atm. In the range of temperature considered (290 up to 330 K), which correspond to *in vivo* conditions, these properties can be treated as constant.

On the other hand, in the same temperature range~~,~~ the diagonal elements of thermal expansion tensor, α_{ii}, display a significant temperature dependence,

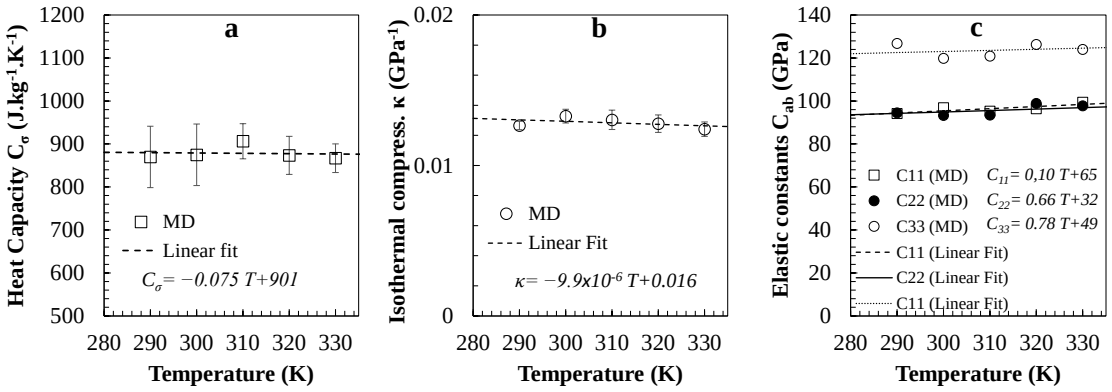

Figure 3: Temperature dependence of (a) the heat capacity at constant stress C_σ, (b) the isothermal compressibility κ and (c) the elastic constants C_{11}, C_{22} and C_{33} (Voigt notation) under 1 atm.

as shown in Fig. 4 (a). The inset in Fig. 4 (a) shows the principal directions of the tensor of thermal expansion computed from the eigenvalues of $\boldsymbol{\alpha}$. In a comparison with the values of the coefficients of thermal expansion in the **x** (11), **y** (22) and **z** (33) directions, it can inferred that these are the principal directions, as expected for a crystal with hexagonal symmetry. This observation is corroborated by ~~the~~ Fig. 2 (f), where the ~~terms~~ off-diagonal of the ~~tensor of~~ thermal expansion fluctuate~~s~~ around zero ~~for~~ after ~~approximated~~ 1 ns, *i.e.* when the simulation converges.

We observe thermal contraction for temperatures exceeding approximately 315 K. The origin of this thermal contraction can be attributed to specific vibration modes observed in layered crystals. The Grüneisen parameter $\gamma_{G,ij}$ quantifies the anharmonicity of the interactions in crystals and can be computed from the heat capacity C_σ, the thermal expansion α_{ij}, and the elastic stiffness constants C_{11}, C_{22} and C_{33} (Voigt notation) [54]:

$$\gamma_{G,ij} = \frac{V}{C_\sigma} C_{ijkl} \alpha_{kl}. \tag{8}$$

For hexagonal crystals, there are only two independent Grüneisen parameters [55]: the in-plane $\gamma_{G,11} = \gamma_{G,22}$ and the out-of-plane $\gamma_{G,33}$ parameters

(the basal plane is defined with respect to the {0001} surface). The results in Fig. 4 (b) shows ~~indeed~~ that the in-plane Grüneisen parameter are approximately equal. On the other hand, the out-of-plane $\gamma_{G,33}$ parameter is larger between 290 and 300 K, ~~which means that in this temperature range~~ there is greater anharmonicity in the **z**-direction than in-plane directions. At 310 K, the anharmonicity in all direction are similar~~,~~ and between 320 and 330 K the in-plane direction displays greater anharmonicity than the out-of-plane direction. In Fig. 5, the pair distribution functions of HAP computed at 290 and 300 K suggest that the thermal contraction in bulk HAP is associated with a slightly increase of the inter-atomic distances between the hydroxyl oxygens (**c**), and between the phosphate oxygens (**d**).

Negative Grüneisen parameters have been observed in layered crystals due to membrane effects [56] ~~as well as~~ in amorphous minerals [57], and they can be attributed to a lateral compression following a strong expansion in the normal direction~~,~~ the ~~so-called~~ Poisson's compression, ~~or due to a negative Grüneisen parameter~~ [58]. Non-monotonous thermal expansion coefficients of HAP-β-tricalcium phosphate ceramics have also been reported in experiments [47].

3.2. HAP-water nanopores

The heat capacities at constant stress C_σ of nanoporous HAP-water systems as a function of the pore size H computed at conditions of 310 K and 1 atm ~~are shown in Fig. 6 as a function of the pore size~~ H. The continuous red line correspond to results obtained using the mixture rule:

$$C_\sigma = f_{HAP} C_{\sigma,HAP} + (1 - f_{HAP}) C_{\sigma,W},$$

where $C_{\sigma,HAP} = 906$ J.kg^{-1}.K^{-1} (see Tab. 2) and $C_{\sigma,SPC/E} = 4513$ J.kg^{-1}.K^{-1} [59] are the bulk values of bulk HAP and SPC/E water (dashed line) at 310 K, respectively, and f_{HAP} is the volume fraction of solid HAP computed from the average pore size (see Section 2.2):

$$f_{HAP} = 1 - \phi = 1 - \frac{\langle H \rangle}{|| \mathbf{c} ||},$$

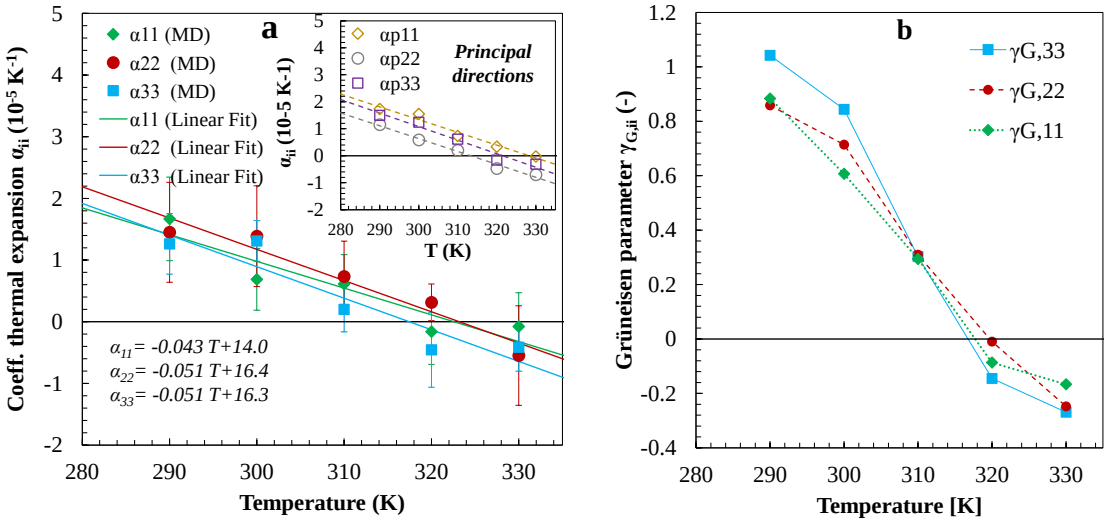

Figure 4: Temperature dependence of (a) the coefficients of thermal expansion and (b) the Grüneisen parameters of bulk HAP under 1 atm. The inset shows the principal values $\alpha_{p,11}, \alpha_{p,22}$ and $\alpha_{p,33}$ of the coefficient of thermal expansion.

where is ϕ the porosity.

The heat capacity of nanoporous HAP computed from the MD simulations, C_σ^{MD}, is larger than the values estimated from the mixture rule with heat capacity of bulk HAP and SPC/E water. Consequently, confinement significantly alters the heat capacity of water.

Using the C_σ^{MD} values computed from MD simulations, we estimated the heat capacity of confined water $C_{\sigma,conf}$ using the mixture rule

$$C^w_{\sigma,conf} = \frac{\left(C^{MD}_\sigma - f_{HAP} C_{\sigma,HAP}\right)}{(1 - f_{HAP})}, \tag{9}$$

(dotted blue line in Fig. 6). The heat capacity of confined water reaches a maximum for the pore size of 6 nm. This non-monotonous variation is closed to the to value of 7 nm measured experimentally in nanoporous silica [14, 15] and, according to and co-workers [16], is due to the bimodal distribution of single molecules enthalpies in liquid water [14, 15].

When compared with bulk ~~water~~, the excess of the heat capacity of confined

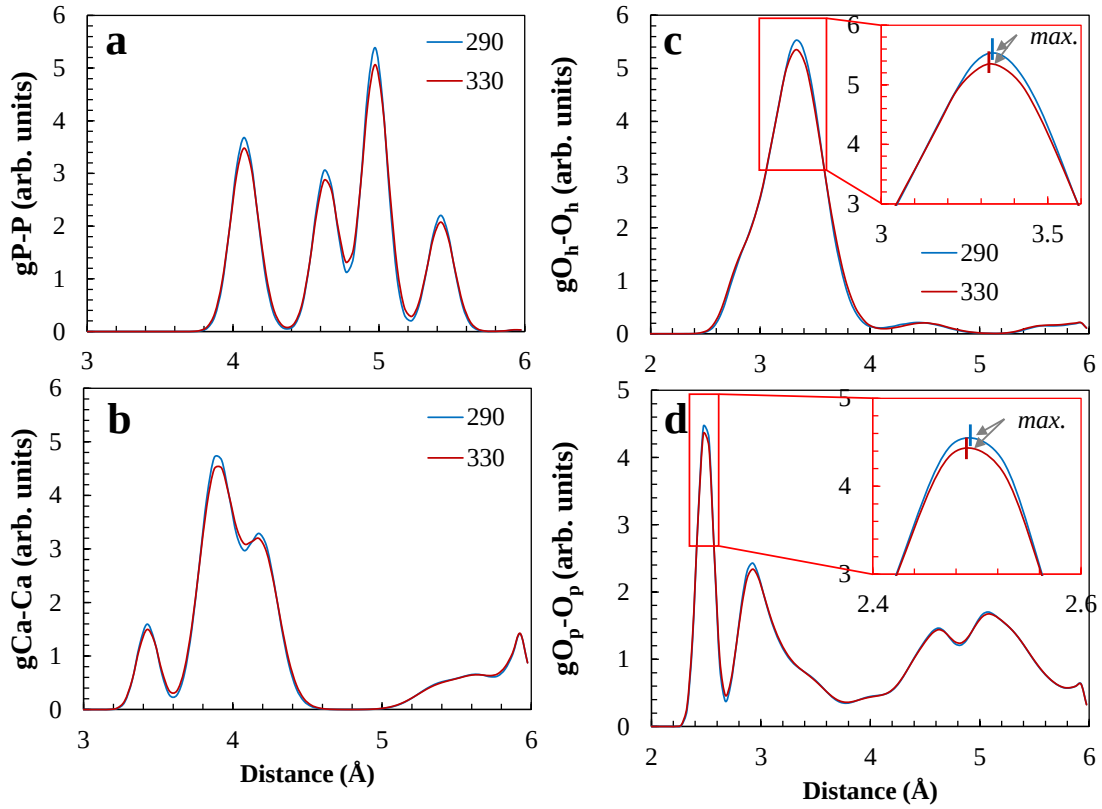

Figure 5: Radial distribution functions g of (a) P-P, (b) Ca-Ca, (c) Oh-Oh (hydroxyl oxygen) and (d) Op-Op (phosphate oxygen) pairs in bulk HAP at 290 and 330 K both under 1 atm. The insets show the distance of the peaks in the g profiles of oxygen decreasing with the temperature.

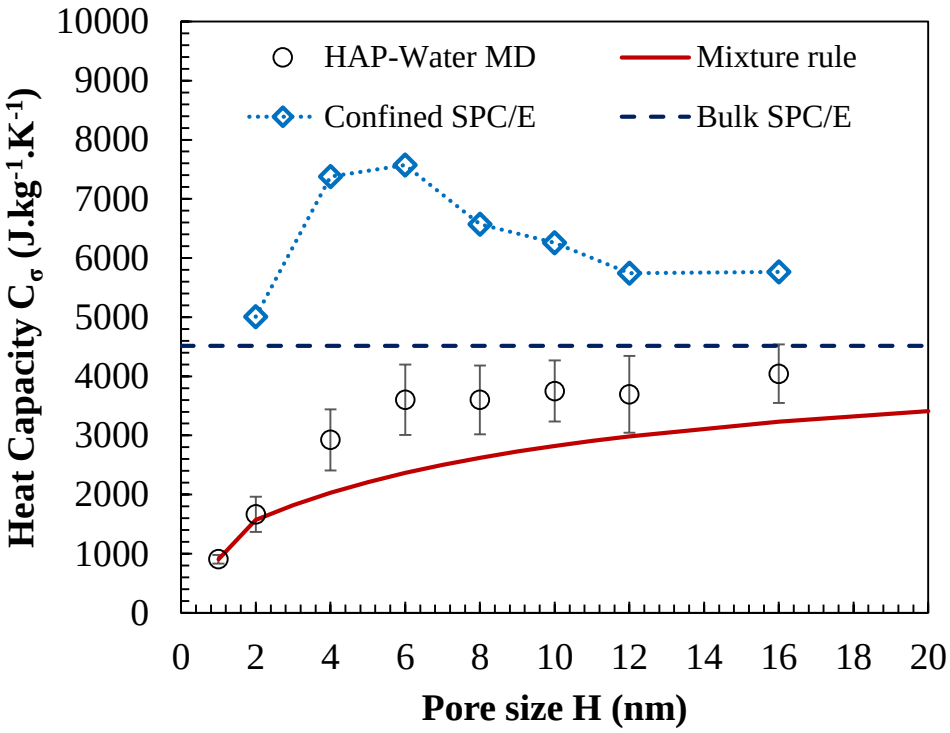

Figure 6: Heat capacity at constant stress C_σ of nanoporous HAP-water systems as a function of the pore size H within *in vivo* (310 K and 1 atm) conditions. Full lines display the results of a mixture rule with the bulk values of the heat capacity of HAP at 310K of $C_{\sigma,HAP}$ =906 J.kg^{-1}.K^{-1} and SPC/E water (dashed line) of $C_{\sigma,SPC/E}$=4513 J.kg^{-1}.K^{-1} [59]. The dotted line display the estimations of the heat capacity of confined water $C_{\sigma,conf}$ computed from the mixture rule: $C_{\sigma,conf} = \left(C_\sigma - f_{HAP} C_{\sigma,HAP}\right)/(1 - f_{HAP})$.

water is on the order of 1000 J.kg^{-1}.K^{-1}. The effects of confinement on the heat capacity of water in nanoporous HAP are not negligible and, therefore, are critical in relevant upscaling modeling approaches.

The coefficients of thermal expansion of HAP-water systems computed at the conditions of 310 K and 1 atm are presented in Fig. 7 as a function of the pore size H. As observed in nanoporous silica [17], the thermal expansion of confined water also depends on the pore size. Here, we also observe that the thermal expansion in the out-of-plane direction is close to the thermal expansion of bulk

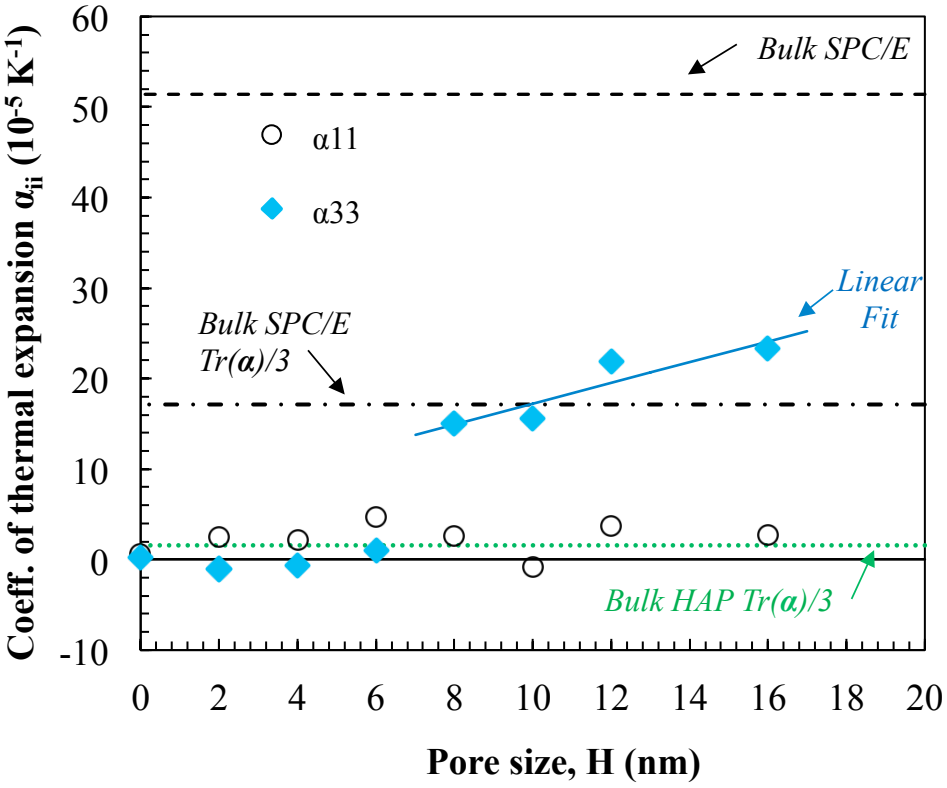

Figure 7: Coefficients of thermal expansion of nanoporous HAP-water systems as a function of the pore size H within *in vivo* (310 K and 1 atm) conditions.

HAP to pore sizes H up to 6 nm. In this case, nanoporous HAP exhibits a out-of-plan thermal expansion typical of a solid close to 10^{-5} K^{-1}. On the other hand, larger pores exhibit the thermal expansion in the out-of-plane direction governed by the thermal expansion of water. In this case, nanoporous HAP exhibits a out-of-plan thermal expansion typical of a liquid like water close to 10^{-4} K^{-1}. This dependence of the thermal expansion on the pore size is ~~expected~~ to impact the macroscopic (effective) thermal expansion of HAP-rich materials and may be used to explain non-linearities in the thermal expansion observed experimentally in porous HAP [60].

~~Figure 7 reports the thermal expansion coefficients of HAP-water as a func-~~

tion of the pore size H , computed at the conditions of 310 K and 1 atm. For nanopores larger than 6 nm, the thermal expansion in the out-of-plane direction, α_{33}, is typical of liquid-like water (close to 10^{-4} K^{-1}). On the other hand, the in-plane and out-of-plane thermal expansion behaviour is similar to that of bulk HAP. This thermal expansion dependence on the nanopore size will impact the macroscopic (effective) thermal expansion of HAP-rich materials and may be used to explain the non-linearity observed in the thermal expansion of porous HAP [60].

3.3. Upscaling the Heat Capacity and Thermal Expansion of HAP

In this section, we present an upscaling strategy to determine the effective heat capacity and effective thermal expansion of porous HAP using as input parameters the heat capacities and thermal expansion coefficients of HAP-water nanopores obtained using MD simulations.

The heat capacity can be extrapolated to other water contents of interest by a rule of mixture because volume (or mass for specific heat capacities) and energy are extensive thermodynamic quantities. However, the significant dependence of the heat capacity on the pore size raises the issues of which value should be adopted in the upscaling procedure. Figure 8 (a) shows the domain of variability of the effective heat capacity of porous hydroxyapatite as a function of the porosity at 310 K and under 1 atm. The the heat capacities of bulk water and of confined water within the 6 nm HAP nanopore were used to define the lower- and upper limits of this domain.

Up-scaling the coefficient of thermal expansion is more complicated than a simple rule of mixture due to the tensorial nature of this property and the dependence on the microstructure. Analytical homogenization techniques present a consistent framework to upscale various intensive quantities and transformation fields resulting of temperature changes [61]. Here, we adopt the simple Voigt (α_V^{eff}) and Reuss (α_R^{eff}) formulas to estimate the effective coefficient of

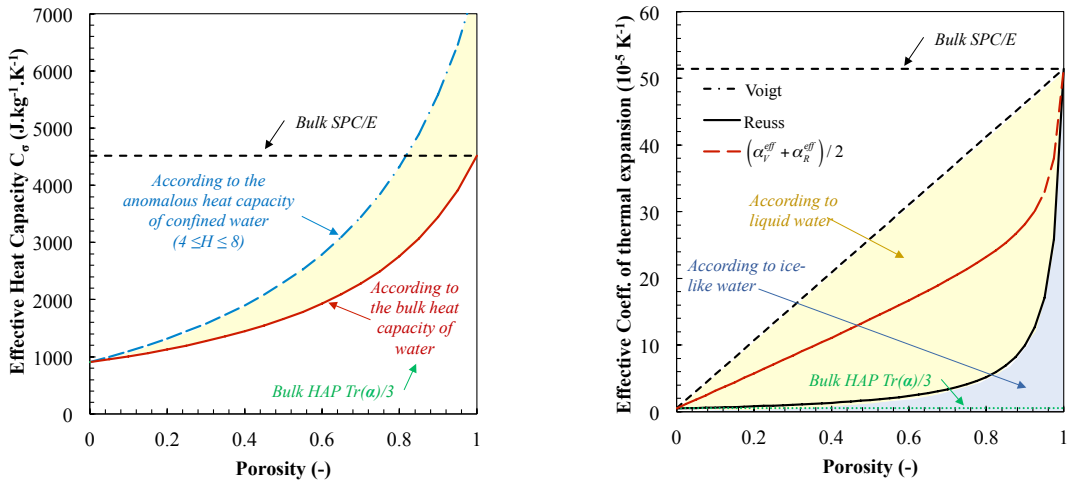

Figure 8: Estimations of the effective (a) heat capacity at constant stress and (b) the coefficients of thermal expansion of saturated HAP-water systems as a function of the porosity at $T = 310$ K and $P = 1$ atm conditions.

thermal expansion [62]:

$$\alpha_V^{eff} = \left\langle \frac{1}{9K_V} C_{p,iikl}\alpha_{p,kl} \right\rangle_\Sigma, \text{where} \quad K_V = \left\langle \frac{1}{9} C_{iijj} \right\rangle_\Sigma, \tag{10}$$

$$\alpha_R^{eff} = \left\langle \frac{1}{3}\mathrm{Tr}(\boldsymbol{\alpha}_p) \right\rangle_\Sigma, \tag{11}$$

where the subscript p stands for a phase in the composite and the operator $\langle\star\rangle_\Sigma$ stands for a volume average over the representative elementary volume Σ. Voigt and Reuss estimations assume constant strains and constant stresses, respectively. These estimates correspond to the bounds of the effective properties of composites. Figure 8 (b) displays the domain of variability of the effective coefficients of thermal expansion as a function of the porosity according to these limities and the particularities of the thermal expansion of confined water within *in vivo* conditions.

4. Discussion

Capturing the physical origin of the heat capacity and thermal expansion of bulk HAP. The heat capacities computed from MD simulation and fluctuation formulas are in agreement with experimental values reported for solid HAP ~~and~~ corroborate the transferability of HAP empirical force fields proposed by de Leeuw and co-workers [35, 36] to compute the thermal properties of ~~HAP.~~ The anisotropic nature of the thermal expansion of bulk HAP was quantified at temperatures corresponding to *in vivo* conditions~~. We observed~~ negative (principal) coefficients of thermal expansion of bulk HAP ~~at~~ temperature exceeding 310 K~~, which~~ represents the first observation of thermal contraction of HAP at temperatures relevant to *in vivo* conditions.

Nanoconfinement affects the heat capacity and thermal expansion of HAP-water. HAP-water nanoporous systems have an effective heat capacity that exceeds the estimates obtained using the heat capacity of bulk water. Our predictions ~~for the heat capacity of confined water~~ shows a non-monotonous behavior with a maximum value for a pore of approximately 7 nm, which is in agreement with the heat capacities obtained for other nanoporous materials [16]. The differences between the heat capacities of bulk water and of water confined in the 7 nm nanopore is very large (1000 $J.kg^{-1}.K^{-1}$) and could be the origin of the variability of macroscopic heat capacity observed experimentally in HAP-rich materials. Similarly, the thermal expansion of confined water exhibited a dependence on the confinement. The coefficients associated with the thermal expansion of HAP-water nanoporous system in the out-of-plane direction are close to the thermal expansion of bulk HAP (close to 10^{-5} K^{-1}) up to nanopores of 6 nm; for larger pores the out-of-plane thermal expansion coefficients corresponds to the the thermal expansion of bulk water (close to 10^{-4} K^{-1}). This dependence on the confinement is expected to impact the macroscopic (effective) thermal expansion of HAP-rich materials.

Nanoscale origin of the variability of thermal properties in porous HAP. Homogenization techniques were used to upscale the heat capacity and the coefficients of thermal expansion of HAP-water nanoporous. The anomalous behavior of confined water leads to significant variability at the macroscopic scale in the thermal properties of HAP materials. This finding indicates that nanoscale processes such as the confinement dependency of water properties are crucial to understand and quantify the variability of properties observed in HAP-rich materials as well as other nanoporous materials. Further, since the confined water properties are pore-size related, experimental measurements of heat capacity and coefficient of thermal expansion provide information on the micro- and mesopore size distributions in HAP.

5. Conclusion

The heat capacity and thermal expansion of bulk HAP and HAP-water nanoporous systems have been computed by means of MD simulations. These thermal properties are crucial to predict the thermo-mechanical behavior of bones and other HAP-rich materials. The simulations were used to assess the effects of temperature in bulk HAP and of confinement in HAP-water thermal properties. This work contributes towards a better understanding of the factors affecting the thermo-mechanical behavior of bones. The identification of nanoscale phenomenon related to the confinement of water as a source of the property variability can be transferred to the study of other nanoporous adsorbing materials. As body fluid and natural water is rich in ions, further work will consider the role of dissolved ions in confined water and their effect on the macroscopic thermal properties of HAP-electrolyte systems.

[1] N. A. S. Taylor, M. J. Tipton, G. P. Kenny, Considerations for the measurement of core, skin and mean body temperatures, Journal of Thermal Biology 46 (2014) 72–101. doi:10.1016/j.jtherbio.2014.10.006.
URL http://www.sciencedirect.com/science/article/pii/S0306456514001521

[2] S. Karmani, The thermal properties of bone and the effects of surgical intervention, Current Orthopaedics 20 (1) (2006) 52–58. doi:10.1016/j.cuor.2005.09.011.
URL http://www.orthopaedicsandtraumajournal.co.uk/article/S0268-0890(05)00167-2/abstract

[3] W. R. Krause, D. W. Bradbury, J. E. Kelly, E. M. Lunceford, Temperature elevations in orthopaedic cutting operations, Journal of Biomechanics 15 (4) (1982) 267–275. doi:10.1016/0021-9290(82)90173-7.
URL http://www.sciencedirect.com/science/article/pii/0021929082901737

[4] G. Augustin, T. Zigman, S. Davila, T. Udilljak, T. Staroveski, D. Brezak, S. Babic, Cortical bone drilling and thermal osteonecrosis, Clinical Biomechanics 27 (4) (2012) 313–325. doi:10.1016/j.clinbiomech.2011.10.010.
URL http://www.clinbiomech.com/article/S0268-0033(11)00278-6/abstract

[5] E. B. Dolan, M. G. Haugh, D. Tallon, C. Casey, L. M. McNamara, Heat-shock-induced cellular responses to temperature elevations occurring during orthopaedic cutting, Journal of The Royal Society Interface 9 (77) (2012) 3503–3513. doi:10.1098/rsif.2012.0520.
URL http://rsif.royalsocietypublishing.org/content/9/77/3503

[6] R. L. Jacobs, R. D. Ray, The effect of heat on bone healing. A disadvantage in the use of power tools, Archives of Surgery (Chicago, Ill.: 1960) 104 (5) (1972) 687–691.

[7] E. Phillips, Greek medicine, Camelot Press Ltd, 1973.

[8] A. R. Eriksson, T. Albrektsson, Temperature threshold levels for heat-induced bone tissue injury: A vital-microscopic study in the rabbit, The Journal of Prosthetic Dentistry 50 (1) (1983) 101–107.

doi:10.1016/0022-3913(83)90174-9.
URL http://www.sciencedirect.com/science/article/pii/0022391383901749

[9] R. Calttenburg, J. Cohen, S. Conner, N. Cook, Thermal properties of cancellous bone, Journal of Biomedical Materials Research Part A 9 (2) (1975) 169–182. doi:10.1002/jbm.820090206.
URL http://onlinelibrary.wiley.com/doi/10.1002/jbm.820090206/full

[10] S. Weiner, W. Traub, Organization of hydroxyapatite crystals within collagen fibrils, FEBS Letters 206 (2) (1986) 262–266.

[11] L. Kuhn, S. J. Eppell, W. Tong, M. J. Glimcher, J. L. Katz, Size and Shape of Mineralites in Young Bovine Bone Measured by Atomic Force Microscopy, Calcified Tissue International 72 (5) (2003) 592–598. doi:10.1007/s00223-002-1077-7.
URL http://link.springer.com/10.1007/s00223-002-1077-7

[12] J. M. Holmes, D. H. Davies, W. J. Meath, R. A. Beebe, Gas Adsorption and Surface Structure of Bone Mineral, Biochemistry 3 (12) (1964) 2019–2024. doi:10.1021/bi00900a042.
URL http://dx.doi.org/10.1021/bi00900a042

[13] I. Brovchenko, A. Oleinikova, Interfacial and Confined Water, Elsevier, 2008.

[14] F. M. Etzler, P. J. White, The heat capacity of water in silica pores, Journal of Colloid and Interface Science 120 (1) (1987) 94–99. doi:10.1016/0021-9797(87)90326-2.
URL http://www.sciencedirect.com/science/article/pii/0021979787903262

[15] F. M. Etzler, J. J. Conners, Temperature dependence of the heat capacity of water in small pores, Langmuir 6 (7) (1990) 1250–1253. doi:10.1021/

la00097a010.
URL http://dx.doi.org/10.1021/la00097a010

[16] F. M. Etzler, R. F. Ross, R. A. Halcomb, The structure and properties of vicinal water: Lessons from statistical geometry, Physica A: Statistical Mechanics and its Applications 172 (1) (1991) 161–173. doi:10.1016/0378-4371(91)90318-7.
URL http://www.sciencedirect.com/science/article/pii/0378437191903187

[17] S. Xu, G. W. Scherer, T. S. Mahadevan, S. H. Garofalini, Thermal Expansion of Confined Water, Langmuir 25 (9) (2009) 5076–5083. doi:10.1021/la804061p.
URL http://dx.doi.org/10.1021/la804061p

[18] T. Honorio, B. Bary, F. Benboudjema, Thermal properties of cement-based materials: Multiscale estimations at early-age, Cement and Concrete Composites 87 (2018) 205–219. doi:10.1016/j.cemconcomp.2018.01.003.
URL http://www.sciencedirect.com/science/article/pii/S0958946516305200

[19] M. J. A. Qomi, F.-J. Ulm, R. J.-M. Pellenq, Physical Origins of Thermal Properties of Cement Paste, Physical Review Applied 3 (6) (2015) 064010. doi:10.1103/PhysRevApplied.3.064010.
URL http://link.aps.org/doi/10.1103/PhysRevApplied.3.064010

[20] T. Lemaire, J. Kaiser, S. Naili, V. Sansalone, Modelling of the transport in electrically charged porous media including ionic exchanges, Mechanics Research Communications 37 (5) (2010) 495–499. doi:10.1016/j.mechrescom.2010.05.009.
URL http://www.sciencedirect.com/science/article/pii/S0093641310000716

[21] T. Honorio, T. Lemaire, D. Di Tommaso, S. Naili, Anomalous water and ion dynamics in hydroxyapatite mesopores, Computational Materials Science.

[22] T. T. Pham, T. Lemaire, E. Capiez-Lernout, M. Lewerenz, Q.-D. To, J. K. Christie, D. D. Tommaso, N. H. d. Leeuw, S. Naili, Properties of water confined in hydroxyapatite nanopores as derived from molecular dynamics simulations, Theoretical Chemistry Accounts 134 (5) (2015) 59. doi:10.1007/s00214-015-1653-3.
URL https://link.springer.com/article/10.1007/s00214-015-1653-3

[23] M. Prakash, T. Lemaire, D. Di Tommaso, N. de Leeuw, M. Lewerenz, M. Caruel, S. Naili, Transport properties of water molecules confined between hydroxyapaptite surfaces: A Molecular dynamics simulation approach, Applied Surface Science 418 (Part A) (2017) 296–301. doi:10.1016/j.apsusc.2017.02.029.
URL http://www.sciencedirect.com/science/article/pii/S016943321730380X

[24] D. Di Tommaso, M. Prakash, T. Lemaire, M. Lewerenz, N. H. de Leeuw, S. Naili, Molecular Dynamics Simulations of Hydroxyapatite Nanopores in Contact with Electrolyte Solutions: The Effect of Nanoconfinement and Solvated Ions on the Surface Reactivity and the Structural, Dynamical, and Vibrational Properties of Water, Crystals 7 (2) (2017) 57. doi:10.3390/cryst7020057.
URL http://www.mdpi.com/2073-4352/7/2/57

[25] M. Prakash, T. Lemaire, M. Caruel, M. Lewerenz, N. H. d. Leeuw, D. D. Tommaso, S. Naili, Anisotropic diffusion of water molecules in hydroxyapatite nanopores, Physics and Chemistry of Minerals 44 (7) (2017) 509–519. doi:10.1007/s00269-017-0878-1.
URL https://link.springer.com/article/10.1007/s00269-017-0878-1

[26] G. Leibfried, W. Ludwig, Theory of Anharmonic Effects in Crystals, in: F. Seitz, D. Turnbull (Eds.), Solid State Physics, Vol. 12, Academic Press,

1961, pp. 275–444. doi:10.1016/S0081-1947(08)60656-6.
URL http://www.sciencedirect.com/science/article/pii/S0081194708606566

[27] T. Cagin, N. Karasawa, S. Dasgupta, W. A. Goddard, Thermodynamic and elastic properties of polyethylene at elevated temperatures, MRS Online Proceedings Library Archive 278.

[28] T. Lee, Monte Carlo Simulations of Structural Phase Transitions in Metals and Alloys, PhD Thesis, Brown University (2010).

[29] J. R. Ray, A. Rahman, Statistical ensembles and molecular dynamics studies of anisotropic solids. II, The Journal of Chemical Physics 82 (9) (1985) 4243–4247. doi:10.1063/1.448813.
URL http://extranet.enpc.fr:3588/doi/abs/10.1063/1.448813

[30] J. R. Ray, Molecular dynamics equations of motion for systems varying in shape and size, The Journal of Chemical Physics 79 (10) (1983) 5128–5130. doi:10.1063/1.445636.
URL http://extranet.enpc.fr:3588/doi/abs/10.1063/1.445636

[31] D. C. Wallace, Thermodynamics of Crystals, Courier Corporation, 1998, google-Books-ID: qLzOmwSgMIsC.

[32] M. P. Allen, D. J. Tildesley, Computer Simulation of Liquids, Oxford University Press, New York, 1989.

[33] K. Sudarsanan, R. A. Young, Significant precision in crystal structural details. Holly Springs hydroxyapatite, Acta Crystallographica Section B: Structural Crystallography and Crystal Chemistry 25 (8) (1969) 1534–1543. doi:10.1107/S0567740869004298.
URL http://scripts.iucr.org/cgi-bin/paper?a06841

[34] D. Mkhonto, N. H. d. Leeuw, A computer modelling study of the effect of water on the surface structure and morphology of fluorapatite: introducing

a Ca10(PO4)6f2 potential model, Journal of Materials Chemistry 12 (9) (2002) 2633–2642. doi:10.1039/B204111A.
URL http://pubs.rsc.org/en/content/articlelanding/2002/jm/b204111a

[35] N. H. de Leeuw, A computer modelling study of the uptake and segregation of fluoride ions at the hydrated hydroxyapatite (0001) surface: introducing a Ca 10 (PO 4) 6 (OH) 2 potential model, Physical Chemistry Chemical Physics 6 (8) (2004) 1860–1866. doi:10.1039/B313242K.
URL http://pubs.rsc.org/en/Content/ArticleLanding/2004/CP/B313242K

[36] N. H. de Leeuw, S. C. Parker, Molecular-dynamics simulation of MgO surfaces in liquid water using a shell-model potential for water, Physical Review B 58 (20) (1998) 13901–13908. doi:10.1103/PhysRevB.58.13901.
URL https://link.aps.org/doi/10.1103/PhysRevB.58.13901

[37] H. J. C. Berendsen, J. R. Grigera, T. P. Straatsma, The missing term in effective pair potentials, The Journal of Physical Chemistry 91 (24) (1987) 6269–6271. doi:10.1021/j100308a038.
URL http://dx.doi.org/10.1021/j100308a038

[38] N. Almora-Barrios, N. H. d. Leeuw, Modelling the interaction of a Hyp-Pro-Gly peptide with hydroxyapatite surfaces in aqueous environment, CrystEngComm 12 (3) (2010) 960–967. doi:10.1039/B917179G.
URL https://pubs.rsc.org/en/content/articlelanding/2010/ce/b917179g

[39] S. E. R. Hernandez, I. Streeter, N. H. d. Leeuw, The effect of water on the binding of glycosaminoglycan saccharides to hydroxyapatite surfaces: a molecular dynamics study, Physical Chemistry Chemical Physics 17 (34) (2015) 22377–22388. doi:10.1039/C5CP02630J.
URL https://pubs.rsc.org/en/content/articlelanding/2015/cp/c5cp02630j

[40] I. T. Todorov, W. Smith, K. Trachenko, M. T. Dove, DL_poly_3 new dimensions in molecular dynamics simulations via massive parallelism, Journal of Materials Chemistry 16 (20) (2006) 1911–1918. doi:10.1039/B517931A.
URL http://pubs.rsc.org/en/content/articlelanding/2006/jm/b517931a

[41] J. R. Ray, Elastic constants and statistical ensembles in molecular dynamics, Computer Physics Reports 8 (3) (1988) 109–151. doi:10.1016/0167-7977(88)90009-3.
URL http://www.sciencedirect.com/science/article/pii/0167797788900093

[42] T. Honorio, L. Brochard, M. Vandamme, Hydration Phase Diagram of Clay Particles from Molecular Simulations, Langmuir 33 (44) (2017) 12766–12776. doi:10.1021/acs.langmuir.7b03198.
URL http://dx.doi.org/10.1021/acs.langmuir.7b03198

[43] M. Parrinello, A. Rahman, Strain fluctuations and elastic constants, The Journal of Chemical Physics 76 (5) (1982) 2662–2666. doi:10.1063/1.443248.
URL http://aip.scitation.org/doi/abs/10.1063/1.443248

[44] T. Kijima, M. Tsutsumi, Preparation and Thermal Properties of Dense Polycrystalline Oxyhydroxyapatite, Journal of the American Ceramic Society 62 (9-10) (1979) 455–460. doi:10.1111/j.1151-2916.1979.tb19104.x.
URL http://onlinelibrary.wiley.com/doi/10.1111/j.1151-2916.1979.tb19104.x/abstract

[45] E. P. Egan, Z. T. Wakefield, K. L. Elmore, High-Temperature Heat Content of Hydroxyapatite, Journal of the American Chemical Society 72 (6) (1950) 2418–2421. doi:10.1021/ja01162a019.
URL https://doi.org/10.1021/ja01162a019

[46] F. J. A. L. Cruz, J. N. Canongia Lopes, J. C. G. Calado, M. E. Minas da Piedade, A Molecular Dynamics Study of the Thermodynamic Properties of Calcium Apatites. 1. Hexagonal Phases, The Journal of Physical Chemistry B 109 (51) (2005) 24473–24479. doi:10.1021/jp054304p.
URL http://dx.doi.org/10.1021/jp054304p

[47] S. Nakamura, R. Otsuka, H. Aoki, M. Akao, N. Miura, T. Yamamoto, Thermal expansion of hydroxyapatite--tricalcium phosphate ceramics, Thermochimica Acta 165 (1) (1990) 57–72. doi:10.1016/0040-6031(90)80206-E.
URL http://www.sciencedirect.com/science/article/pii/004060319080206E

[48] F. J. A. L. Cruz, J. N. Canongia Lopes, J. C. G. Calado, Molecular Dynamics Study of the Thermodynamic Properties of Calcium Apatites. 2. Monoclinic Phases, The Journal of Physical Chemistry B 110 (9) (2006) 4387–4392. doi:10.1021/jp055808q.
URL https://doi.org/10.1021/jp055808q

[49] W. Y. Ching, P. Rulis, A. Misra, Ab initio elastic properties and tensile strength of crystalline hydroxyapatite, Acta Biomaterialia 5 (8) (2009) 3067–3075. doi:10.1016/j.actbio.2009.04.030.
URL http://www.sciencedirect.com/science/article/pii/S1742706109001949

[50] R. Snyders, D. Music, D. Sigumonrong, B. Schelnberger, J. Jensen, J. M. Schneider, Experimental and ab initio study of the mechanical properties of hydroxyapatite, Applied Physics Letters 90 (19) (2007) 193902. doi:10.1063/1.2738386.
URL http://aip.scitation.org/doi/abs/10.1063/1.2738386

[51] R. F. S. Hearmon, A. A. Maradudin, An Introduction to Applied Anisotropic Elasticity, Physics Today 14 (1961) 48. doi:10.1063/1.

3057153.
URL http://adsabs.harvard.edu/abs/1961PhT....14j..48H

[52] S. Lees, F. Rollins Jr., Anisotropy in hard dental tissues, Journal of Biomechanics 5 (6) (1972) 557–564. doi:10.1016/0021_9290(72)90027-9.
URL http://www.sciencedirect.com/science/article/pii/0021929072900279

[53] R. S. Gilmore, J. L. Katz, Elastic properties of apatites, Journal of Materials Science 17 (4) (1982) 1131–1141. doi:10.1007/BF00543533.
URL https://link.springer.com/article/10.1007/BF00543533

[54] J. S. Dugdale, D. K. C. MacDonald, The Thermal Expansion of Solids, Physical Review 89 (4) (1953) 832–834. doi:10.1103/PhysRev.89.832.
URL https://link.aps.org/doi/10.1103/PhysRev.89.832

[55] G. Grimvall, Thermophysical Properties of Materials, Elsevier, 1999, google-Books-ID: jfP4CePrv6QC.

[56] I. Lifshitz, Thermal properties of chain and layered structures at low temperatures, Zh. Eksp. Teor. Fiz 22 (4) (1952) 475–486.

[57] J. Fabian, P. B. Allen, Thermal Expansion and Gr\"uneisen Parameters of Amorphous Silicon: A Realistic Model Calculation, Physical Review Letters 79 (10) (1997) 1885–1888. doi:10.1103/PhysRevLett.79.1885.
URL https://link.aps.org/doi/10.1103/PhysRevLett.79.1885

[58] N. A. Abdullaev, Grüneisen parameters for layered crystals, Physics of the Solid State 43 (4) (2001) 727–731. doi:10.1134/1.1366002.
URL https://doi.org/10.1134/1.1366002

[59] Y. Mao, Y. Zhang, Thermal conductivity, shear viscosity and specific heat of rigid water models, Chemical Physics Letters 542 (2012) 37–41. doi:10.1016/j.cplett.2012.05.044.
URL http://www.sciencedirect.com/science/article/pii/S0009261412006367

[60] G. R. Fischer, P. Bardhan, J. E. Geiger, The lattice thermal expansion of hydroxyapatite, Journal of Materials Science Letters 2 (10) (1983) 577–578. doi:10.1007/BF00719864.
URL https://link.springer.com/article/10.1007/BF00719864

[61] G. J. Dvorak, Y. Benveniste, On Transformation Strains and Uniform Fields in Multiphase Elastic Media, Proceedings of the Royal Society of London A: Mathematical, Physical and Engineering Sciences 437 (1900) (1992) 291–310. doi:10.1098/rspa.1992.0062.
URL http://rspa.royalsocietypublishing.org/content/437/1900/291

[62] R. deWit, Elastic constants and thermal expansion averages of a nontextured polycrystal, Journal of Mechanics of Materials and Structures 3 (2) (2008) 195–212. doi:10.2140/jomms.2008.3.195.
URL https://msp.org/jomms/2008/3-2/p01.xhtml